2025 IEEE Conference on Control Technology and Applications (CCTA)
August 25 - 27, 2025. San Diego, CA, USA

Robust Temperature Estimation in All-Solid-State Batteries

Patryck Ferreira and Shu-Xia Tang

Abstract— **This paper proposes a robust observer for temperature estimation in All-Solid-State Batteries (ASSBs) based on a coupled electrochemical-thermal model. The thermal subsystem is modeled using a quintuple-state structure that captures the temperature dynamics of five key components: the cathode, electrolyte, anode, and the surfaces near the cathode and anode. The thermal model is driven by electrochemical heat generation, which is derived from a physics-based electrochemical model, in which the cathode diffusion coefficient depends on the cathode temperature. To ensure robustness under modeling uncertainties, the observer gain is designed such that the estimation error dynamics achieve D-stability, constraining the observer poles to lie within a prescribed disk in the complex plane. For simulation purpose, a piecewise time-discretized implementation of the coupled model is adopted. Simulation results under the Urban Dynamometer Driving Schedule (UDDS) demonstrate the accuracy of the proposed temperature observer and its robustness to parameter uncertainties, demonstrating its potential for reliable thermal monitoring and enhanced safety in ASSBs.**

Index Terms— **All-Solid-State Batteries, Robust Temperature Observer, Time-Varying Diffusion Coefficient, Electrochemical-Thermal Coupling.**

I. Introduction

ASSBs represent a significant advancement in energy storage, employing solid electrolytes to achieve higher energy density than conventional lithium-ion batteries [1]. Unlike conventional lithium-ion batteries, ASSBs eliminate the need for flammable liquid electrolytes, thereby reducing the risk of fire and explosion [2].

To better understand the performance of ASSBs, modeling approaches have been developed. For example, [3] proposed a one-dimensional model to simulate ASSB performance. In [4], finite element methods were used to model ASSBs, capturing both electrochemical processes and damage evolution. [5] presented a model for micro ASSBs, supported by electrochemical experiments for accurate parameter characterization. Additionally, a reduced-order electrochemical model was proposed in [6] using Padé approximation and polynomial approximations of concentration distributions. [7] introduced a quintuple thermal model for ASSBs, enabling temperature modeling of five key components.

Regarding estimation in ASSBs, available references are limited. For instance, [7] estimated temperatures in different ASSB components using a Kalman filter. [8] proposed a Kalman Filter for ASSB State-of-Charge (SoC) estimation, while [9] introduced an extended Kalman filter for SoC estimation based on Li-ion concentration. [10] applied a PDE disturbance estimator and a backstepping state estimator to electrolyte concentration in batteries. [11] presented a quintuple-layer thermal observer for ASSBs that accounts for thermal conductivity uncertainties using adaptive estimation.

In this paper, the main contributions are:

- To the best of the authors' knowledge, this is the first work to model the cathode diffusion and temperature as fully coupled processes in ASSBs, unlike [11], which used a cascaded approach.
- Unlike [7], which did not consider modeling uncertainties, this work explicitly incorporates structured uncertainties in thermal parameters and sensor measurements.
- To the best of the authors' knowledge, this is the first application of a D-stability-based robust observer for temperature estimation in ASSBs, enabling simultaneous estimation of the cathode, electrolyte, anode, and their respective surface temperatures.

The remainder of this paper is organized as follows: Section II introduces the thermal model. Section III describes the electrochemical model. Section IV details the robust observer design. Section V discusses simulation results, and Section VI concludes the paper with future work directions.

II. Thermal model

Figure 1 presents a schematic diagram of a ASSB. The structure consists of three main regions: the cathode on the left, the solid electrolyte in the middle, and the anode on the right. Li^+ move from the anode to the cathode during discharge and in the reverse direction during charge. The system is driven by an external current $I(t)$, and the voltage across the cell is denoted by $V(t)$. Convective heat exchange with ambient air occurs at both ends of the battery.

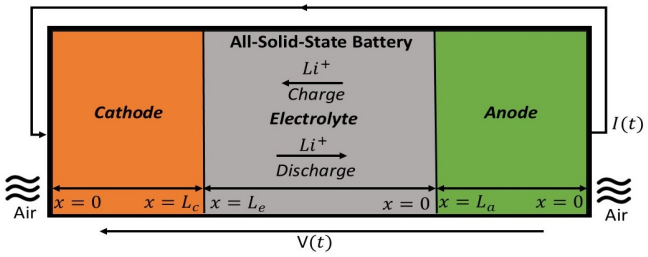

Fig. 1: All-Solid-State Battery.

The thermal model incorporates five ODEs for temperature, each corresponding to one of the internal components of the battery (cathode, solid electrolyte, anode), as well as for the surfaces (one near the anode and another near the

P. Ferreira and S.-X. Tang are with the Department of Mechanical Engineering, Texas Tech University, Lubbock, USA. patferre@ttu.edu, shuxia.tang@ttu.edu.

2025 IEEE Conference on Control Technology and Applications (CCTA) | 979-8-3315-3908-5/25/$31.00 ©2025 IEEE | DOI: 10.1109/CCTA53793.2025.11151409

cathode). The quintuple thermal model, as presented in [7], is described by the following system.

$$\dot{\mathbf{T}}(t) = (\mathcal{A} + \Delta\mathcal{A})\mathbf{T}(t) + B\mathbf{u}(t), \tag{II.1}$$

$$y(t) = (\mathbf{c} + \Delta\mathbf{c})\mathbf{T}(t), \tag{II.2}$$

where

$$\mathcal{A} = \begin{bmatrix} \frac{-R_{\mathrm{c}} - R_{\mathrm{air}}}{\lambda_{\mathrm{air}} R_{\mathrm{c}} R_{\mathrm{air}}} & \frac{1}{\lambda_{\mathrm{air}} R_{\mathrm{c}}} & 0 & 0 & 0 \\ \frac{1}{\lambda_{\mathrm{c}} R_{\mathrm{c}}} & \frac{-1}{\lambda_{\mathrm{c}}} & 0 & 0 & 0 \\ 0 & \frac{1}{\lambda_{\mathrm{e}} R_{\mathrm{e}}} & \frac{-1}{\lambda_{\mathrm{e}} R_{\mathrm{e}}} & 0 & 0 \\ 0 & 0 & \frac{1}{\lambda_{\mathrm{a}} R_{\mathrm{e}}} & \frac{-1}{\lambda_{\mathrm{a}} R_{\mathrm{e}}} & 0 \\ 0 & 0 & 0 & \frac{1}{\lambda_{\mathrm{air}} R_{\mathrm{a}}} & \frac{R_{\mathrm{a}} - R_{\mathrm{air}}}{\lambda_{\mathrm{air}} R_{\mathrm{a}} R_{\mathrm{air}}} \end{bmatrix}, \tag{II.3}$$

$$\mathbf{T}(t) = \begin{bmatrix} T_{\mathrm{s}^-}(t) & T_{\mathrm{c}}(t) & T_{\mathrm{e}}(t) & T_{\mathrm{a}}(t) & T_{\mathrm{s}^+}(t) \end{bmatrix}^{\mathrm{tr}}, \tag{II.4}$$

$$B = \begin{bmatrix} \frac{1}{\lambda_{\mathrm{air}} R_{\mathrm{air}}} & 0 & 0 & 0 & \frac{-1}{\lambda_{\mathrm{air}} R_{\mathrm{air}}} \\ 0 & \frac{1}{\lambda_{\mathrm{c}}} & \frac{1}{\lambda_{\mathrm{e}}} & \frac{1}{\lambda_{\mathrm{a}}} & 0 \end{bmatrix}^{\mathrm{tr}}, \tag{II.5}$$

$$\mathbf{u}(t) = \begin{bmatrix} T_{\mathrm{air}}(t) & S(t) \end{bmatrix}^{\mathrm{tr}}, \tag{II.6}$$

$$\mathbf{c} = \begin{bmatrix} 0 & 0 & 0 & 0 & 1 \end{bmatrix}. \tag{II.7}$$

Here, the subscripts $\mathrm{s}^-, \mathrm{c}, \mathrm{e}, \mathrm{a}, \mathrm{s}^+$ and air represent the surfaces near the cathode, the cathode, the electrolyte, the anode, the surface near the anode, and air, respectively. R denotes thermal resistance, and $\lambda = v\rho c_p$, where v is the volume, ρ is the density, and c_p is the specific heat capacity. The vector $\mathbf{T}(t)$ represents the system's temperatures, $\mathbf{u}(t)$ denotes the inputs, and $S(t)$ represents the heat generated by electrochemical reactions, as described in [7]:

$$S(t) = V(t)I(t), \tag{II.8}$$

in which the terminal voltage is computed from the electrochemical model introduced in Section III. $\Delta\mathcal{A}$ and $\Delta\mathbf{c}$ are unknown parameters that represent time-varying uncertainties, modeled as follows [12]:

$$\begin{bmatrix} \Delta\mathcal{A} \\ \Delta\mathbf{c} \end{bmatrix} = \begin{bmatrix} M_1 \\ \mathbf{m}_2 \end{bmatrix} \Xi N, \tag{II.9}$$

where M_1, $\mathbf{m}_2$, and N are known constant real matrices, and Ξ is an unknown real matrix that satisfies:

$$\Xi\Xi^{\mathrm{tr}} \leq I. \tag{II.10}$$

M_1 captures variations in thermal properties (e.g., conductivity and volume fluctuations), while $\mathbf{m}_2$ models sensor-related uncertainties such as calibration drift. The matrix N distributes these uncertainties across the state variables.

Remark II.1. *In [7], the uncertainties $\Delta\mathcal{A}$ and $\Delta\mathbf{c}$ were not considered, and the model was validated through Ansys Transient Thermal Analysis. However, in this work, these uncertainties are explicitly incorporated to account for parameter variations.*

III. Electrochemical model

The dynamics of Li^+ concentration within the cathode are governed by Fick's second law, resulting in a Partial Differential Equation (PDE) that describes the diffusion process in the active material, as detailed in [6]:

$$\frac{\partial c_{\mathrm{s}}^-}{\partial t}(t,x) = D_{\mathrm{s}}^-(T_c(t))\frac{\partial^2 c_{\mathrm{s}}^-}{\partial x^2}(t,x), \ t > 0, \ x \in (0, L_{\mathrm{c}}), \tag{III.1}$$

$$D_{\mathrm{s}}^-(T_c(t))\frac{\partial c_{\mathrm{s}}^-(t, L_c)}{\partial x} = \frac{I(t)}{FA}, \quad t > 0, \quad x \in (0, L_{\mathrm{c}}), \tag{III.2}$$

$$D_{\mathrm{s}}^-(T_c(t))\frac{\partial c_{\mathrm{s}}^-(t, 0)}{\partial x} = 0, \quad t > 0, \quad x \in (0, L_{\mathrm{c}}), \tag{III.3}$$

$$c_{\mathrm{s}}^-(0,x) = c_{\mathrm{s},0}^-(x), \quad x \in [0, L_{\mathrm{c}}], \tag{III.4}$$

where c_{s}^- is the concentration of Li^+ in the cathode, $D_{\mathrm{s}}^-(T(t_c))$ is the diffusion coefficient, F is Faraday's Constant, A is the surface area [3]. Due to the high exchange current density of metallic lithium, the charge transfer overpotential at the anode is negligible, allowing the anode's charge transfer kinetics to be omitted [10].

The diffusion coefficient $D_{\mathrm{s}}^-(T_c(t))$ is a function with Arrhenius-like dependence, inherently influenced by temperature [13], as follows:

$$D_s^-(T_c(t)) = D_{\mathrm{s}}^-(T_c(0))e^{E_{D_{\mathrm{s}}^-}\frac{T_c(t) - T_c(0)}{T_c(t)T_c(0)}}, \tag{III.5}$$

$E_{D_s}^-$ represents the activation energy coefficient.

The main ionic transport mechanisms in the $\mathrm{Li_3PO_4}$ solid electrolyte are diffusion and migration of Li^+. This process is described by [6]:

$$\frac{\partial c_{\mathrm{e}}}{\partial t}(t,x) = \frac{2D_{\mathrm{Li}}^+ D_{\mathrm{n}}^-}{D_{\mathrm{Li}}^+ + D_{\mathrm{n}}^-}\frac{\partial^2 c_{\mathrm{e}}}{\partial x^2}(t,x) + r(c_{\mathrm{e}}(t,x)), \quad t > 0, \quad x \in (0, L_{\mathrm{e}}), \tag{III.6}$$

$$\frac{\partial c_{\mathrm{e}}(t,0)}{\partial x} = -\frac{I(t)}{2FAD_{\mathrm{Li}}^+}, \quad t > 0, \quad x \in (0, L_{\mathrm{e}}), \tag{III.7}$$

$$\frac{\partial c_{\mathrm{e}}(t,L_e)}{\partial x} = -\frac{I(t)}{2FAD_{\mathrm{Li}}^+}, \quad t > 0, \quad x \in (0, L_{\mathrm{e}}), \tag{III.8}$$

$$c_{\mathrm{e}}(0,x) = \delta c_{\mathrm{e},0}(x), \quad x \in [0, L_{\mathrm{e}}], \tag{III.9}$$

where c_{e} is the concentration in the electrolyte, D_{Li^+} and D_{n^-} are the diffusion coefficients of Li^+ and n^- in the solid electrolyte, δ is the fraction of free Li^+ in equilibrium, and r represents the net generation of charge carriers, and it is neglected here.

The charge transfer overpotential at the positive electrode, the mass transfer overpotential caused by the flow of Li^+ in the solid-state electrolyte, and the diffusion overpotential in the interface of the intercalation electrode combine to form the battery's total overpotential, which is denoted by [6]:

$$\eta_{\mathrm{t}}(t) = \eta_{\mathrm{ct}}(t) + \eta_{\mathrm{mt}}(t) + \eta_{\mathrm{d}}(t). \tag{III.10}$$

A simplified version of η_{ct} is given by [9]:

$$\eta_{\mathrm{ct}}(t) = \frac{2RT}{F}\sinh\left(\frac{-I(t)}{2i_{0,\mathrm{pos}}(t)}\right), \tag{III.11}$$

where

$$i_{0,\text{pos}}(t) = FAk_{\text{pos}} \left(\frac{(c_{\text{s,max}}^{-} - c_{\text{s}}^{-}(L_{\text{c}},t))c_{\text{e}}(L_{\text{e}},t)}{(c_{\text{s,max}}^{-} - c_{\text{s,min}}^{-})c_{\text{s},0}} \right)^{\alpha_{\text{pos}}} \times \left(\frac{(c_{\text{s}}^{-}(L_{\text{c}},t) - c_{\text{s,min}}^{-})}{(c_{\text{s,max}}^{-} - c_{\text{s,min}}^{-})} \right)^{1-\alpha_{\text{pos}}}. \quad \text{(III.12)}$$

Here $c_{\text{s,max}}^{-}$ is the maximum concentration in the cathode and $c_{\text{s,min}}^{-}$ is the minium concentration in cathode.

The mass-transfer overpotential η_{mt} and the diffusion overpotential η_{d} are given by [9], as follows:

$$\eta_{\text{mt}}(t) = \frac{L_e RTI(t)}{c_{\text{e}}F^2A(D_{Li^+} + D_{n^-})}, \quad \text{(III.13)}$$

$$\eta_{\text{d}}(t) = E_{\text{eq}}(\theta_s(t)) - E_{\text{eq}}(\bar{\theta}_s(t)). \quad \text{(III.14)}$$

Here, E_{eq} represents the equilibrium potential. The terminal voltage is given by [9]:

$$V(t) = E_{\text{eq}}(\bar{\theta}_s(t)) + \eta_{\text{l}}(t). \quad \text{(III.15)}$$

This electrochemical model and the thermal model in Section II together present a coupled electrochemical-thermal model, in which the electrochemical heat generation serves as the input to the thermal model, and the cathode diffusion coefficient depends on the cathode temperature. For simulation purposes in Section V, we implement the coupled system in a piecewise time-discretized manner, resulting in a simplified cascaded framework. Specifically, the externally applied current $I(t)$, $t \in [t_i, t_{i+1})$, serves as the input to the electrochemical model described in Section III, which computes the terminal voltage $V(t)$ for all $t \in [t_i, t_{i+1})$. This voltage, along with the current $I(t)$ over the same interval, determines the electrochemical heat generation term $S(t)$ for all $t \in [t_i, t_{i+1})$, which is then used in the thermal model presented in Section II. The quintuple thermal model simulates the temperature evolution, yielding the temperature profile $\mathbf{T}(t)$ for $t \in [t_i, t_{i+1})$. These temperature states are then injected into the electrochemical model as updated parameters for the subsequent time interval $[t_{i+1}, t_{i+2})$, and the process repeats iteratively.

IV. Robust Temperature Estimation in ASSBs

The full order state observer for the system (II.1)-(II.2) is given by:

$$\dot{\hat{T}}(t) = (\mathcal{A} + \Delta\mathcal{A})\hat{T}(t) + B\mathbf{u}(t) + L[y(t) - (\mathbf{c} + \Delta\mathbf{c})\hat{T}(t)], \quad \text{(IV.1)}$$

where L is the observer gain matrix to be designed.

The error state is given by $e(t) = T(t) - \hat{T}(t)$, and the error dynamics is

$$\dot{e}(t) = [\mathcal{A} + \Delta\mathcal{A} - L(\mathbf{c} + \Delta\mathbf{c})]\, e(t). \quad \text{(IV.2)}$$

D-stability refers to the property that all eigenvalues of a dynamic system lie within a prescribed region of the complex plane. The following theorem guarantees the D-stability of the observer error dynamics. It consolidates and streamlines the results of Lemma 1, Theorem 1, and Theorem 2 from [12] into a unified and more accessible form.

Theorem 1. Define a disk in the complex plane by $D(q,r) := \{z \in \mathbb{C} \mid |z - q| < r\}$, where q is a negative scalar design parameter defining the center of the disk and $r > 0$ is the radius. Assume there exist a positive scalar $\epsilon > 0$, a sufficiently small positive constant δ, and a positive definite matrix $Q > 0$, such that the following conditions hold:

$$\epsilon NQN^{\text{tr}} < I, \quad \text{(IV.3)}$$

$$\mathcal{A}_{cq}\left[Q + QN^{\text{tr}}\left(\frac{1}{\epsilon}I - NQN^{\text{T}}\right)^{-1}NQ\right]\mathcal{A}_{cq}^{\text{tr}} + \frac{1}{\epsilon}(M_1 - L\mathbf{m}_2)(M_1 - L\mathbf{m}_2)^{\text{tr}} - r^2Q + \delta I = 0, \quad \text{(IV.4)}$$

$$-\Psi + \Theta^{\text{T}}\Sigma^{-1}\Theta \geq 0, \quad \text{(IV.5)}$$

where $\mathcal{A}_{cq} = \mathcal{A} - L\mathbf{c} - qI$, and

$$L = \Theta^{\text{tr}}\Sigma^{-1} - UW\Sigma^{-1/2}. \quad \text{(IV.6)}$$

Here, $U \in \mathbb{R}^{n\times p}$ satisfies $UU^{\text{tr}} = -\Psi + \Theta^{\text{tr}}\Sigma^{-1}\Theta$, and $W \in \mathbb{R}^{p\times p}$ is an arbitrary matrix, with p being the rank of $-\Psi + \Theta^{\text{tr}}\Sigma^{-1}\Theta$, and

$$\Pi := Q + QN^{\text{tr}}\left(\frac{1}{\epsilon}I - NQN^{\text{tr}}\right)^{-1}NQ, \quad \text{(IV.7)}$$

$$\Sigma := \mathbf{c}\Pi\mathbf{c}^{\text{tr}} + \frac{1}{\epsilon}\mathbf{m}_2\mathbf{m}_2^{\text{tr}}, \quad \text{(IV.8)}$$

$$\Theta := \mathbf{c}\Pi(\mathcal{A} - qI)^{\text{tr}} + \frac{1}{\epsilon}\mathbf{m}_2M_1^{\text{tr}}, \quad \text{(IV.9)}$$

$$\Psi := (\mathcal{A} - qI)\Pi(\mathcal{A} - qI)^{\text{tr}} + \frac{1}{\epsilon}M_1M_1^{\text{tr}} - r^2Q + \delta I. \quad \text{(IV.10)}$$

Under these conditions, by choosing the observer gain as L, the observer error $e(t)$ governed by the dynamics in (IV.2) is guaranteed to be D-stable; that is, all poles of the observer error dynamics lie within the prescribed disk $D(q,r)$, ensuring robustness and satisfactory transient response in the presence of parameter uncertainties.

Proof. The proof of this theorem can be referred to the proofs of Lemma 1, Theorem 1, and Theorem 2 in [12]. □

As stated in [12], an observer is regarded as robust when its estimation error dynamics remain stable under all admissible parameter uncertainties, ensuring asymptotic convergence of the estimation error. By adopting a D-stability-based design that constrains the poles of the error dynamics within a prespecified stability region, the proposed observer in this work guarantees robustness and achieves the desired transient performance, even in the presence of structured uncertainties in thermal parameters and measurement errors.

Similarly, for simulation purposes in Section V, we implement it in a piecewise time-discretized manner, resulting in a simplified cascaded framework. Specifically, the robust

observer estimates the internal temperatures $\hat{\mathbf{T}}(t)$ for all $t \in [t_i, t_{i+1})$. Then, the estimated cathode temperature $\hat{T}_{\mathrm{c}}(t)$, defined for all $t \in [t_i, t_{i+1})$, is used to compute the temperature-dependent diffusion coefficient $D_{\mathrm{s}}^{-}(\hat{T}_{\mathrm{c}}(t))$ for all $t \in [t_i, t_{i+1})$. The estimated terminal voltage $\hat{V}(t)$ for all $t \in [t_i, t_{i+1})$, computed from the electrochemical model described in Section III, along with the current $I(t)$ over the same interval, determines the estimated electrochemical heat generation term $\hat{S}(t)$ for all $t \in [t_i, t_{i+1})$, which is then used in the thermal observer for $t \in [t_{i+1}, t_{i+2})$. The process repeats iteratively. Note that an open-loop observer configuration for the system (III.1)-(III.4) is used, where the estimated cathode temperature is plugged into the electrochemical model without feedback correction to the plant.

V. Simulation Results

Simulations were performed in MATLAB on an MSI laptop equipped with an Intel Core i7 2.4 GHz CPU and 32 GB of RAM. Thermal resistances between internal components were calculated using the standard relation $R = \frac{L}{kA}$, where L is the length, k is the thermal conductivity, and A is the cross-sectional area. Thermal resistances for the cathode, electrolyte, and anode were calculated individually to ensure accurate modeling of heat transfer within the ASSB. The anode is composed of metallic lithium, the cathode is based on traditional $LiCoO_2$, while the electrolyte consists of amorphous Li_3PO_4, which separates the anode from the cathode. The Equilibrium potential E_{eq} in the $LiCoO_2$ cathode is calculated as [6]:

$$E_{\mathrm{eq}}(\theta_s(t)) = \frac{\begin{array}{c}(-219.027 + 322.003\theta_s^2 - 198.242\theta_s^4 \\ + 354.911\theta_s^6 - 467.8070\theta_s^8 + 207.168\theta_s^{10})\end{array}}{\begin{array}{c}(-44.337 + 36.643\theta_s^2 - 3.430\theta_s^4 \\ + 113.081\theta_s^6 - 182.567\theta_s^8 + 80.3097\theta_s^{10})\end{array}}.$$

The electrochemical and thermal parameters used in the simulations are listed in Table I and are based on values reported in [7].

The battery was simulated as a 100 mAh cell using the UDDS current profile shown in Figure 2 [14].

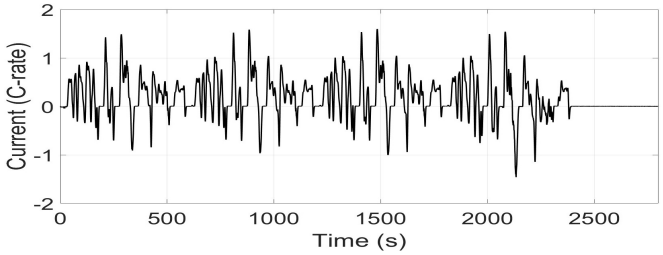

Fig. 2: Current profile used in the UDDS simulation.

TABLE I: Electrochemical and thermal parameters used in the simulations

Parameter	Symbol	Value and Unit
Electrochemical Parameters		
Electrode area	A	$0.0001\,\mathrm{m}^2$
Max. lithium concentration	$c_{\mathrm{s,max}}^{-}$	$2.33 \times 10^4\,\mathrm{mol\ m}^{-3}$
Min. lithium concentration	$c_{\mathrm{s,min}}^{-}$	$1.1645 \times 10^4\,\mathrm{mol\ m}^{-3}$
Initial electrolyte concentration	$c_{e,0}$	$6.01 \times 10^4\,\mathrm{mol\ m}^{-3}$
Li-ion diffusivity in electrolyte	D_{Li}^{+}	$0.9 \times 10^{-15}\,\mathrm{m}^2\mathrm{s}^{-1}$
Li diffusivity in cathode	D_s^{-}	$1.76 \times 10^{-15}\,\mathrm{m}^2\mathrm{s}^{-1}$
Li diffusivity in anode	D_n^{-}	$5.1 \times 10^{-15}\,\mathrm{m}^2\mathrm{s}^{-1}$
Faraday constant	F	$96485.3365\,\mathrm{C\ mol}^{-1}$
Electrolyte thickness	L_{e}	$1.5 \times 10^{-6}\,\mathrm{m}$
Electrode thickness	L_{p}	$3.2 \times 10^{-7}\,\mathrm{m}$
Transfer coefficient (cathode)	α_{pos}	0.6
Reaction rate constant (anode)	k_{n}	$1 \times 10^{-2}\,\mathrm{m}^3\mathrm{mol}^{-1}\mathrm{s}^{-1}$
Reaction rate constant (cathode)	k_{p}	$5.1 \times 10^{-4}\,\mathrm{m}^3\mathrm{mol}^{-1}\mathrm{s}^{-1}$
Thermal Parameters		
Density of anode	ρ_{a}	$534\,\mathrm{kg\ m}^{-3}$
Density of electrolyte	ρ_{e}	$710\,\mathrm{kg\ m}^{-3}$
Density of cathode	ρ_{c}	$4790\,\mathrm{kg\ m}^{-3}$
Specific heat of anode	c_{pa}	$3600\,\mathrm{J\ kg}^{-1}\mathrm{K}^{-1}$
Specific heat of electrolyte	c_{pe}	$1252\,\mathrm{J\ kg}^{-1}\mathrm{K}^{-1}$
Specific heat of cathode	c_{pc}	$730\,\mathrm{J\ kg}^{-1}\mathrm{K}^{-1}$
Thermal conductivity of anode	k_{a}	$85\,\mathrm{W\ m}^{-1}\mathrm{K}^{-1}$
Thermal conductivity of electrolyte	k_{e}	$0.7\,\mathrm{W\ m}^{-1}\mathrm{K}^{-1}$
Thermal conductivity of cathode	k_{c}	$3.7\,\mathrm{W\ m}^{-1}\mathrm{K}^{-1}$

A. Uncertainty in the Thermal Model

The structured uncertainty perturbations introduced into the thermal model, $\Delta\mathcal{A}$ and $\Delta\mathbf{c}$, are defined as:

$$\Delta\mathcal{A} = 10^{-3}\times \begin{bmatrix} 0.0010 & 0.2010 & 0 & 0 & 0 \\ 0.0010 & 0.2010 & 0 & 0 & 0 \\ 0 & 0.1000 & 0.1000 & 0 & 0 \\ 0 & 0 & 0.1000 & 0.1000 & 0 \\ 0 & 0 & 0 & 0.1000 & 0.1000 \end{bmatrix},$$

$$\Delta\mathbf{c} = \begin{bmatrix} 0 & 0 & 0 & 0 & 0.0025 \end{bmatrix}.$$

The perturbations $\Delta\mathcal{A}$ and $\Delta\mathbf{c}$ were chosen to reflect realistic uncertainty levels in ASSB thermal models, with magnitudes on the order of 10^{-3}. These small but meaningful variations capture effects from thermal resistance, material property fluctuations, and sensor inaccuracies. The structure of $\Delta\mathcal{A}$ reflects layered heat transfer, while $\Delta\mathbf{c}$ captures sensor error, especially near the outermost layers. This formulation ensures physical relevance and numerical stability in the observer design.

The matrix $M_1 \in \mathbb{R}^{5\times5}$ captures the sensitivity of the system matrix A to thermal parameter uncertainties, such as conductivity and interface resistance. Nonzero elements were set to 0.01 to reflect small but realistic variations, affecting primarily adjacent layers in the solid-state battery.

$$M_1 = \begin{bmatrix} 0.01 & 0.01 & 0 & 0 & 0 \\ 0.01 & 0.01 & 0 & 0 & 0 \\ 0 & 0.01 & 0.01 & 0 & 0 \\ 0 & 0 & 0.01 & 0.01 & 0 \\ 0 & 0 & 0 & 0.01 & 0.01 \end{bmatrix}. \tag{V.1}$$

The matrix $\mathbf{m}_2 \in \mathbb{R}^{1\times5}$ models sensor uncertainty. As only the anode-side temperature is measured, $\mathbf{m}_2$ includes a single

nonzero element (0.25) to represent typical sensor error.

$$\mathbf{m}_2 = \begin{bmatrix} 0 & 0 & 0 & 0 & 0.25 \end{bmatrix}. \tag{V.2}$$

In theory, Ξ is unknown and only assumed to satisfy the norm-bounded condition $\Xi\Xi^{\text{tr}} \leq I$. However, for simulation purposes, we generate a specific Ξ satisfying this condition to test the observer's robustness under structured, bounded uncertainty. A factor of 0.1 was used to limit perturbation effects and preserve numerical stability. This choice ensures that the resulting perturbations $\Delta\mathcal{A}$ and $\Delta\mathbf{c}$ remain within a physically realistic range (on the order of 10^{-3}), consistent with expected variations in thermal parameters and sensor behavior.

$$\Xi = 0.1 \times \begin{bmatrix} 1 & 1 & 0 & 0 & 0 \\ 0 & 1 & 0 & 0 & 0 \\ 0 & 0 & 1 & 0 & 0 \\ 0 & 0 & 0 & 1 & 0 \\ 0 & 0 & 0 & 0 & 1 \end{bmatrix}. \tag{V.3}$$

The matrix $N \in \mathbb{R}^{5\times5}$ distributes uncertainty across battery layers. The entries $N(1,1)$, $N(1,2)$, $N(5,4)$, and $N(5,5)$ are set to 0.001 to represent minimal uncertainty near the cathode and anode surfaces. In contrast, the diagonal values in the internal layers (e.g., cathode, electrolyte, anode) are set to higher values to reflect greater thermal variability:

$$N = \begin{bmatrix} 0.001 & 0.001 & 0 & 0 & 0 \\ 0 & 0.1 & 0 & 0 & 0 \\ 0 & 0 & 0.1 & 0 & 0 \\ 0 & 0 & 0 & 0.1 & 0 \\ 0 & 0 & 0 & 0.001 & 0.001 \end{bmatrix}. \tag{V.4}$$

The matrix N ensures that uncertainty is distributed across battery layers in a physically consistent way, reflecting known variations in material properties and sensor accuracy in ASSBs.

B. True Model Temperature

Figure 3 shows the simulated terminal voltage $V(t)$ obtained by using the cathode temperature T_{c} as input to the diffusion equation (III.5). The voltage profile reflects the dynamic response of the battery under the UDDS current profile. This behavior confirms that the model correctly captures the coupling between electrochemical and thermal dynamics, with the overall voltage trend decreasing due to cumulative capacity consumption and the high-frequency fluctuations corresponding to changes in the applied current.

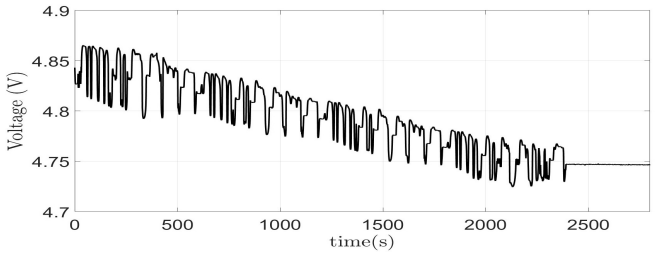

Fig. 3: Voltage using T_{c}.

The thermal model defined in (II.1)-(II.2) is considered the true thermal model for the simulations. Figure 4 shows the simulated temperatures of different ASSB regions: cathode surface T_{s^-}, cathode T_{c}, electrolyte T_{e}, anode T_{a}, and anode surface T_{s^+} during the UDDS current profile. Initially, all regions start near the ambient temperature of 25°C. As current is applied, temperatures rise due to Joule heating, electrochemical reactions, and interfacial resistances.

The electrolyte T_{e} consistently shows the lowest temperature, which is attributed to its low thermal conductivity (0.7 W $\text{m}^{-1}\text{K}^{-1}$) and central position between the cathode and anode, allowing some heat dissipation to both sides. The cathode T_{c}, made of $LiCoO_2$, reaches intermediate temperatures due to its moderate thermal conductivity (3.7 W $\text{m}^{-1}\text{K}^{-1}$) and partial exposure to convective cooling at the cathode surface. The highest temperatures occur at the anode T_{a} and anode surface T_{s^+} despite lithium metal's high thermal conductivity (85 W $\text{m}^{-1}\text{K}^{-1}$), likely due to poor convective cooling on the anode side and significant interfacial resistance at the anode–electrolyte boundary. These results highlight how material properties, geometry, and boundary conditions together govern the temperature distribution within the ASSB.

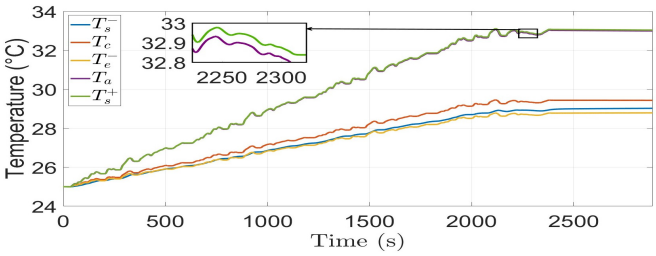

Fig. 4: Temperatures in different regions of the ASSB.

C. Observer Estimation

Building upon the true model, a robust observer was implemented to estimate the thermal states of the battery in real time. Figure 5 shows the estimated terminal voltage $\hat{V}(t)$ obtained by using the estimated cathode temperature $\hat{T}_{\text{c}}$ as input to the diffusion equation (III.5). The voltage profile exhibits a dynamic response nearly identical to that obtained with the true cathode temperature T_{c}, confirming the accuracy and robustness of the temperature estimation framework. The close agreement between the profiles demonstrates that the proposed observer effectively captures the cathode thermal dynamics, enabling precise voltage prediction despite uncertainties in the temperature estimate.

Figure 6 compares the temperature states estimated by the observer with the true system temperatures. To quantify the observer performance, the Root Mean Square Error (RMSE) between the estimated and true temperatures was computed for all thermal states. The results are: Temperature RMSE $= [0.2014,\ 0.2083,\ 0.2561,\ 0.1863,\ 0.1861]$ °C, corresponding to $\hat{T}_{\text{s}^-}$, $\hat{T}_{\text{c}}$, $\hat{T}_{\text{e}}$, $\hat{T}_{\text{a}}$, and $\hat{T}_{\text{s}^+}$, respectively.

The observer's ability to accurately estimate the internal temperatures despite the presence of structured uncertainties

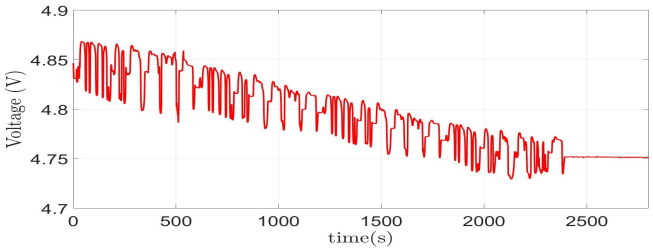

Fig. 5: Voltage using $\hat{T}_c$.

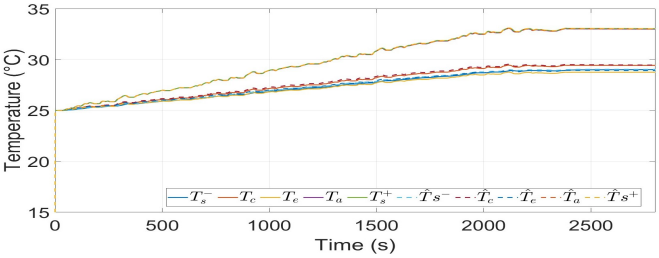

Fig. 6: Comparison of true and estimated temperature states in the ASSB.

$\Delta\mathcal{A}$ and $\Delta\mathbf{c}$ demonstrates its robustness. The small RMSE values across all thermal states confirm that the observer maintains high estimation accuracy even with realistic variations in thermal parameters and measurement inaccuracies. This validates the D-stability-based design's effectiveness in ensuring stable and reliable estimation under bounded modeling errors and sensor disturbances.

VI. Conclusion

This paper developed a coupled electrochemical–thermal estimation framework for ASSBs, employing a cascaded structure that maintains coupling through the dependence of the diffusion coefficient on the estimated cathode temperature. A robust observer based on D-stability theory was designed to estimate the quintuple internal temperatures under structured uncertainties, ensuring accurate thermal state estimation despite parameter variations and modeling errors. The estimated cathode temperature was directly substituted into the cathode diffusion model to compute the temperature-dependent diffusion coefficient, forming an open-loop observer configuration without feedback correction. Simulation results under the UDDS current profile demonstrated excellent agreement between the true and estimated temperature profiles, with low RMSE values confirming the accuracy and robustness of the proposed framework. These findings highlight the potential of the developed estimation approach for improving thermal monitoring and enhancing the safety of ASSBs.

Future work will focus on designing a coupled observer for the coupled electrochemical-thermal model. Additionally, experimental validation with ASSB cells will be explored to assess the framework's performance under practical conditions.

References

[1] Yuki Kato, Satoshi Hori, Toshiya Saito, Kota Suzuki, Masaaki Hirayama, Akio Mitsui, Masao Yonemura, Hideki Iba, and Ryoji Kanno. High-power all-solid-state batteries using sulfide superionic conductors. *Nature Energy*, 1(4):1–7, 2016.

[2] Takeshi Uyama, Takao Inoue, and Kazuhiko Mukai. Realizing the ultimate thermal stability of a lithium-ion battery using two zero-strain insertion materials. *ACS Applied Energy Materials*, 1(10):5712–5717, 2018.

[3] D Danilov, RAH Niessen, and PHL Notten. Modeling all-solid-state li-ion batteries. *Journal of the Electrochemical Society*, 158(3):A215, 2010.

[4] Reza Behrou and Kurt Maute. Numerical modeling of damage evolution phenomenon in solid-state lithium-ion batteries. *Journal of The Electrochemical Society*, 164(12):A2573, 2017.

[5] Steve D Fabre, Delphine Guy-Bouyssou, Pierre Bouillon, Frédéric Le Cras, and Charles Delacourt. Charge/discharge simulation of an all-solid-state thin-film battery using a one-dimensional model. *Journal of The Electrochemical Society*, 159(2):A104, 2011.

[6] Zhongwei Deng, Xiaosong Hu, Xianke Lin, Le Xu, Jiacheng Li, and Wenchao Guo. A reduced-order electrochemical model for all-solid-state batteries. *IEEE Transactions on Transportation Electrification*, 7(2):464–473, 2020.

[7] Patryck Ferreira and Shu-Xia Tang. Quintuple thermal model for all-solid-state batteries and temperature estimation through a cascaded thermal-electrochemical model. In *2024 IEEE Conference on Control Technology and Applications (CCTA)*, pages 716–721. IEEE, 2024.

[8] Youngki Kim, Xianke Lin, Armin Abbasalinejad, Sun Ung Kim, and Seung Hyun Chung. On state estimation of all solid-state batteries. *Electrochimica Acta*, 317:663–672, 2019.

[9] Kushagra Upreti, Isaiah Oyewole, Xianke Lin, and Youngki Kim. On simplification of a solid-state battery model for state estimation. In *2019 IEEE Conference on Control Technology and Applications (CCTA)*, pages 487–492. IEEE, 2019.

[10] Dong Zhang, Shu-Xia Tang, Luis D. Couto, and Venkatasubramanian Viswanathan. PDE observer for all-solid-state batteries via an electrochemical model. In *2021 IEEE Conference on Control Technology and Applications (CCTA)*, pages 51–56, 2021.

[11] Patryck Ferreira and Shu-Xia Tang. Adaptive estimation of all-solid-state battery temperatures with thermal conductivity uncertainties. In *2025 American Control Conference (ACC)*. IEEE, 2025.

[12] Zidong Wang and Heinz Unbehauen. Robust state observer design guaranteeing d-stability. *International Journal of Systems Science*, 29(12):1417–1426, 1998.

[13] Reinhardt Klein, Nalin A Chaturvedi, Jake Christensen, Jasim Ahmed, Rolf Findeisen, and Aleksandar Kojic. Electrochemical model based observer design for a lithium-ion battery. *IEEE Transactions on Control Systems Technology*, 21(2):289–301, 2012.

[14] Scott J Moura, Federico Bribiesca Argomedo, Reinhardt Klein, Anahita Mirtabatabaei, and Miroslav Krstic. Battery state estimation for a single particle model with electrolyte dynamics. *IEEE Transactions on Control Systems Technology*, 25(2):453–468, 2016.